PCCP

Spectroscopic characterization of neptunium(VI), plutonium(VI), americium(VI) and neptunium(V) encapsulated in uranyl nitrate hexahydrate

Xiaojuan Yu[1,§]; Jeffrey D. Einkauf[2,§]; Vyacheslav S. Bryantsev[2]; Michael C. Cheshire[2]; Benjamin J. Reinhart[3]; Jochen Autschbach[1]; and Jonathan D. Burns[4]

[1]Department of Chemistry, University at Buffalo, State University of New York, Buffalo, New York 14260, USA
[2]Chemical Sciences Division, Oak Ridge National Laboratory, P.O. Box 2008, Oak Ridge, TN 37831, USA
[3]X-Ray Sciences Division, Argonne National Laboratory, Argonne, IL 60439, USA
[4]Nuclear Engineering and Science Center, Texas A&M University, College Station, TX 77843, USA

For submission to publish in the
Physical Chemistry Chemical Physics
as a Research article.

Spectroscopic characterization of neptunium(VI), plutonium(VI), and americium(VI) and neptunium(V) encapsulated in uranyl nitrate hexahydrate

Spectroscopic characterization of neptunium(VI), plutonium(VI), americium(VI) and neptunium(V) encapsulated in uranyl nitrate hexahydrate

Xiaojuan Yu[1,§]; Jeffrey D. Einkauf[2,§]; Vyacheslav S. Bryantsev[2]; Michael C. Cheshire[2,†]; Benjamin J. Reinhart[3]; Jochen Autschbach[*,1]; and Jonathan D. Burns[*,4]

[1]Department of Chemistry, University at Buffalo, State University of New York, Buffalo, NY 14260, USA
[2]Chemical Sciences Division, Oak Ridge National Laboratory, P.O. Box 2008, Oak Ridge, TN 37831, USA
[3]X-Ray Sciences Division, Argonne National Laboratory, Lemont, IL 60439, USA
[4]Nuclear Engineering and Science Center, Texas A&M University, College Station, TX 77843, USA

*e-mail: burns.jon@tamu.edu, jochena@buffalo.edu

Abstract:

The coordination of crystalline products resulting from the co-crystallization of Np(VI), Pu(VI), Am(VI), and Np(V) with uranyl nitrate hexahydrate (UNH) has been revealed through solid-state spectroscopic characterization via diffuse reflectance UV-Vis-NIR, SEM-EDS, and extended X-ray absorption fine structure (EXAFS). Density functional and multireference wavefunction calculations were performed to analyze the $An(VI/V)O_2(NO_3)_2 \cdot 2H_2O$ electronic structures and to help assign the observed transitions in the absorption spectra. EXAFS show similar coordination between the U(VI) in $UO_2(NO_3)_2 \cdot 6H_2O$ and Np(VI) and Pu(VI); while Am resulted in a similar coordination to Am(III), as reduction occurred prior to EXAFS data was obtained. The co-crystallization of the oxidized transuranic species—penta- and hexavalent—with UNH, represents a significant advance from not only a practical standpoint in providing an elegant solution for used nuclear fuel (UNF) recycle, but also as an avenue to expand the fundamental understanding of the 5f electronic behavior in the solid-state.

Introduction:

There is a profound fascination with the chemistry of the 5f elements, emphasized by many high-profile publications on the topic.[1–24] But 5f elements retain many mysteries and our current understanding of their properties and chemical behavior is limited. On the applications side, the separation of actinides is extremely important in the used nuclear fuel (UNF) cycle; however, a number of considerations must be addressed, specifically the separation schemes, their scale-up, and implementation to an industrial process. A suitable scheme needs to achieve several goals including: (1) ease of implementation for a wide range of fuel types; (2) meet nuclear nonproliferation and safeguard standards; (3) reduce and minimize waste inevitably bound for disposal in a geological repository; and (4) the recovery of usable species, such as several of the actinide (An) elements, to attain maximum energy utilization.[25–27] The obvious target An species include U and Pu, which are the major energy producing constituents. However, Np and Am should also be included, as they significantly increase the long-term hazards and heat-load requirements

of a geologic disposal site.[28–32] Understanding the behavior of these actinide ions during the separation process is critical to facilitate development of separation technologies, and computational quantum chemistry combined with experiments provides an excellent platform to achieve this goal.

The theoretical modeling of actinide ions hinges upon the ability to develop a reliable model of the species in various environments and the necessity of chemical accuracy to correlate with experimental results.[33,34] The use of computational methods in this field has driven our understanding in a wide range of concepts from uranyl bonding in binary systems such as oxides and nitrides to actinide covalency with designed ligands during solvent extraction. In the case of the actinyl species ($An(VI)O_2^{2+}$, $An(VI)$ = U, Np, Pu, Am), the high charge induces strong polarization effects on the environment, coupled with ion pairing interactions with nitrate and water ligands, highlights the importance to design a proper model to describe the complexes in company with a computational protocol taking into account the environment. Another challenging aspect is the proper treatment of the electronic structure of the actinide complex itself, which has a direct result on the accuracy and identification of An species during extraction. Along those lines, spin-orbit (SO) coupling effects are required to account for excited-states calculations and are computationally demanding, but crucial for an accurate representation of electronic transitions. For systems in which relativistic effects are strong, scalar and SO effects should be taken into account for a correct description of actinide compounds. We have chosen to use scalar all-electron relativistic time-dependent DFT (TD-DFT) linear response theory and multi-reference wavefunction theory with SO coupling for this study, which is a suitable combination for predictive modeling of properties in complex actinide systems.[35]

Of the many separation technologies available, a solvent extraction approach is currently the most feasible for the separation and recovery of U and Pu. This is the envelope under which the Plutonium Uranium Reduction-EXtraction (PUREX) process and its variations operate.[36] Unfortunately, these approaches based on solvent extraction have only realized a margin of success when aimed at including Np and Am in the separation. The inability to sufficiently handle Np and Am, instigated an effort world-wide to develop a separations scheme to address this problem. Solvent extraction has moved to the forefront in this initiative,[36,37] while investigations into ion exchange[38–40] have also been carried out. As technical advances have occurred, they have been accompanied by process complexity and added cost, which has prevented implementation on a larger scale.[41]

From this, a challenge has recently been issued to develop a technology which can be adapted into a single-step separation process for recovering U through Am simultaneously, namely, the so-called Group ActiNide EXtraction (GANEX) type process.[42,43] To answer this challenge, a number of methodologies relying on solvent extraction[44–48], ion exchange[38,40,49,50] or crystallization[51–53], have been pursued to accomplish a GANEX-type process. One commonality of the different approaches is the employment of highly oxidizing environments to produce the hexavalent states of U to Am. This is a nontrivial problem for Am, because the reduction potential of $Am(VI)/Am(III)$ is +1.7 V vs normal hydrogen electrode (NHE)[54], making it the most challenging hexavalent An species to generate and stabilize. A variety of methods for attaining $Am(VI)$, have been studied intently. Probably the most widely implemented is the chemical oxidant sodium bismuthate, as it results in near quantitative production of $Am(VI)$.[44,46,51,54]

We have also engaged in this vein of research, aiming at a GANEX-type separation. Our approach, employs co-crystallization as a first step, following the dissolution of UNF in hot HNO_3, to recover all of the hexavalent An(VI) within the UNH lattice.[51,55,56] A near proportional removal of the transuranic (TRU) species to that of U, 1:1 U:TRU, has been observed when the TRUs exist in the hexavalent state, as the actinyl dioxo cation, AnO_2^{2+}.[51] A remarkable yield was observed in the range of 80–90% for this single-step approach, while achieving separation factors of >81 from common contaminant species like Cs^+, Sr^{2+}, Nd^{3+}, and Zr^{4+}, all generated as fission products during the nuclear fission reaction.[52] Preliminary characterization of the crystalline phase utilizing solid-state diffuse reflectance UV-Vis-NIR absorption spectroscopy, has shown the An(VI) species of the TRUs to be present in the crystalline phase.[55] This first-of-its-kind study of the hexavalent TRUs encapsulated in a stable matrix, included initial observation of Np(V) and Am(VI) absorption bands in the solid state. However, no attempt was made to assign the observed transitions band or provide a description of the electronic structure of the TRU species. We have also been able to demonstrate not only are the An(VI) present in the crystalline phase, but they can be efficiently recovered and are homogeneously distributed throughout the solid.[56]

The absorption spectra of actinides, in particular the internal f-f transitions, has found wide use for identification in the visible and UV regions. These transitions for actinide elements are much more intense and broader than those observed for lanthanides, due to crystal field effects,[35] and provide an excellent means of identification, particularly in co-crystallization scheme. Generating accurate electronic spectra of hexavalent actinides will provide a diagnostic tool to identify ions entrained in the crystalline materials. Identification of hexavalent species through solid state absorbance spectra of the crystalline solids will allow for direct identification and speciation of complexed actinide ions and relative quantification of oxidation states. Furthermore, the theoretical analysis will be building upon previous studies to provide an understanding of the chemical bonding of hexavalent actinides in a solid matrix.

Herein, we focus on characterizing the previously reported[55] transitions in the electronic structure of oxidized actinides by systematically filling the 5f orbitals in a series of co-crystallizations with Np(VI), Pu(VI), Am(VI), or Np(V) entrained in a UNH matrix. Assignment of the transitions were accomplished through DR UV-Vis-NIR absorption spectroscopy coupled with theoretical calculations. The theoretical work offers an important avenue to understand the electronic structure, chemical bonding and spectroscopic properties of the targeted complexes. Further characterization of the co-crystallized samples through SEM-EDS and EXAFS enhances the fundamental understanding of the 5f electrons in the solid state.

Experimental:

Materials

Nitric acid (69–70% Omni Trace, HNO_3) was purchased from EDM; sodium bismuthate (ACS Grade, $NaBiO_3$) was purchased from Alfa Aesar; uranyl nitrate hexahydrate (99+%, $UO_2(NO_3)_2 \cdot 6H_2O$) was purchased from Strem Chemicals and all were used as received. Deionized (DI) H_2O was obtained from an ELGA LabWater Purelab Flex ultrapure laboratory water purification system operated at $18.2\ M\Omega\ cm$ at 25 °C. Neptunium-237 oxide (≥99.99+%,

[237]NpO$_2$), and plutonium-239 oxide (≥99.92%, [239]PuO$_2$), and americium-243 oxide (≥99.98%, [243]AmO$_2$), were purchased from the U.S. Department of Energy's National Isotope Development Center and were each converted to the nitrate form by dissolving in nitric acid under moderate heating (~60–90 ºC). **WARNING:** [237]Np, [239]Pu, and [243]Am are all highly radioactive and were handled under ALARA principles in laboratories equipped to handle radioactive materials appropriately. Radiological fume hoods and glove boxes were employed.

Crystallization

The co-crystallization of Np(VI) Pu(VI), and Am(VI) with UNH has been described in detail elsewhere,[51,55,56] but an abbreviated description will be provided as follows. In general, approximately 100 mg of uranyl nitrate (UN) solid was heated to roughly 50–60 ºC in the presents of HNO$_3$ in a temperature-controlled sand bath, which was regulated by a hot plate equipped with a thermocouple temperature monitored. Following the dissolution of all the UN solid (*ca.* 4 h of heating), slow cooling of the system to ambient temperature (~25 ºC) was achieved by cutting power to the hot plate and allowing the sample to cool naturally inside the sand bath. As the system cooled, crystallization occurred slowly. The conditions for each crystallization experiment are summarized in Table 1. At ambient temperature, the crystalline phase was separated from the liquid supernate by centrifugation with a Costar® Spin-X® 0.45 µm cellulose acetate centrifuge tube filter with a mini-centrifuge. For studies investigating hexavalent TRU species, Np(VI), Pu(VI), or Am(VI), 3–4 mg of NaBiO$_3$ was included in the UN solid to ensure the oxidation occurred and was maintained throughout the process. An aliquot of ~1–2.5 mg An(VI) species dissolved in HNO$_3$ was added to the UNH-NaBiO$_3$ mixture. For experiments involving Am(VI), only glass containers, pipettes, and cuvettes were used, as Am(VI) is a very strong oxidant and will react readily with available organic reductants; this includes plastic surfaces. In these cases, decantation was used rather than centrifugation to separate the phases.

Table 1: Experimental conditions for the co-crystallizations of individual TRUs with UNH.

TRU Species	$V_{15.8\ M\ HNO3}$ /µL	V_{H2O} /µL	$V_{58ºC}$ /µL	$[HNO_3]_{58ºC}$ /M	U /mg	[237]Np /mg	[239]Pu /mg	[243]Am /mg
U(VI)-only	2.00	58.0	91.1	0.35	37.6	-	-	-
Np(VI)	5.34	15.7	61.9	1.4	33.5	2.5 (2.2)	-	-
Pu(VI)	16.7	16.3	42.2	6.3	21.7	-	1.1 (1.1)	-
Am(VI)	20.4	20.4	114	2.8	75.3	-	-	1.0 (1.2)
Np(V)	0.13	20.8	44.0	0.047	32.1	1.5 (1.4)	-	-

*Data in parentheses from γ-ray spectroscopy analysis.

Oxidation and Spectral Analysis

The oxidation state and concentrations of the actinides in solution were determined by observing the optical spectra using an Ocean Optics QEPro UV–vis spectrometer and Ocean Optics Flame-NIR NIR spectrometer, an Ocean Optics HL-2000 halogen light source, and a path length of 1 cm. The data were obtained with OceanView analysis software from Ocean Optics and baseline-corrected with OriginPro 2018 Software. The concentration of the UO_2^{2+} was calculated by implementing Beer's Law with the molar extinction coefficient (ε) of 5.47 L mol^{-1} cm^{-1} at 415 nm.[57] The concentration of the NpO_2^{2+} was calculated with an ε of 41 L mol^{-1} cm^{-1} at 1221 nm.[58] The concentration of the PuO_2^{2+} was calculated with an ε of 450 L mol^{-1} cm^{-1} at

830 nm.[59] The concentration of the AmO_2^{2+} was calculated with an ε of 100 L mol^{-1} cm^{-1} at 996 nm.[54] The concentration of the NpO_2^+ was calculated by with an ε of 372 L mol^{-1} cm^{-1} at 980 nm.[58] Quantitative analysis was performed via gamma (γ)-ray spectroscopy using a calibrated Canberra Model GC4018 high-purity germanium detector (HPGe) with an active detector volume of ~45 cm^3 and Lynx^{TM} digital signal analyzer (DSA, Canberra Industries Inc., Meriden, CT). The detector has an energy resolution of 0.925 keV at 122 keV and 1.8 keV at 1300 keV. Relevant nuclear data were obtained from Browne and Firestone.[60] All calibrations were determined with a ^{152}Eu standard γ-ray source traceable to the National Institute of Standards and Technology (NIST) purchased from Eckert & Ziegler Isotope Products. The ^{237}Np was tracked by using the 86.5 keV and 143 keV γ-rays. The ^{239}Pu was tracked semi-quantitatively by using the 59.5 keV γ-ray from ^{241}Am, a decay daughter of the minor isotope ^{241}Pu (0.012% w/w ^{41}Pu/^{239}Pu).

Extended X-ray Absorption Fine Structure Measurements

Small portions of the crystalline phase were directly loaded into the Extended X-ray Absorption Fine Structure (EXAFS) Measurements sample holder as summarized in Table 2. The EXAFS sample holders were made up of a 11.57 mm $\times$ 6.4 mm $\times$ 1.4 mm (OD $\times$ ID $\times$ h) aluminum (5052-H34) washer with 1 mil Kapton adhesive tape (2.5 mil overall thickness) on either side of the washer to contain the sample. The taped washer was then placed inside of a 4 mil LDPE heat-sealed bag, which was then placed inside a 2.5 mil transparent Mylar heat-sealed bag.

Table 2: Summary of EXAFS samples generated.

TRU Species	U /mg	^{237}Np /μg	^{239}Pu /μg	^{243}Am /μg
U(VI)-only	1.66	-	-	-
Np(VI)	7.65	(700)	-	-
Pu(VI)	8.12	-	(180)	-
Am(VI)	0.0927	-	-	(1.8)
Np(V)	3.88	(210)	-	-

*Data in parentheses from γ-ray spectroscopy analysis.

EXAFS measurements were performed at the Advanced Photon Source (APS) at the 12-BM station at Argonne National Laboratory. EXAFS data were acquired at each L_3 edge Np, Pu, and Am (17.610 keV, 18.057 keV, 18.510 keV, respectively) in fluorescence mode at room temperature using a 13-element germanium detector while the U data (L_3 edge of 17.166 keV) were able to be taken in transmission mode. 12-BM uses a double crystal monochromator with Si (111) crystals as well as a 1.1-meter-long flat mirror along with a 1.0-meter toroidal mirror to focus and steer the beam to the samples in the experimental station. The Zr K edge was used to calibrate the energy at 17.998 keV using a Zr foil near the U L_3 edge. Three-to-five 15 min scans were averaged for each sample. The data were processed and modeled using the *ATHENA* and *ARTEMIS* software based on the *IFEFFIT* code from the Demeter 0.9.26 program package.[73] The EXAFS spectra for actinyl ions were modeled starting from the crystal structure of the uranyl $[UO_2(NO_3)_2(H_2O)_2]\cdot4H_2O$ complex[74] and substituting U for Np and Pu. Am data were modelled based on the crystal structure of the trivalent samarium $[Sm(NO_3)_2(H_2O)_4]^+$ complex.[75] Fitting of the data was done over a range of 3.5 to 8.5 (Np, Pu) and 9.5 Å^{-1} (U) and 2.5–8.5 Å^{-1} (Am) in k-space and 1–3 Å in R space. Due to degradation of Np, Pu, and Am-containing samples by radiolysis and other effects, resulted in a limited usable *k*-range and the number of independent

parameters that can be varied, only two-shell O_{ax},O_{eq} (axial, equatorial) models for actinyl species and a single O shell model for Am were considered. The amplitude reduction factor ($S_o^2 = 0.92$) and the coordination numbers (CN) were fixed to their respective values in the crystal structures during fitting,[74,75] while the remaining variables were allowed to float. With these constrains, the model generated physically reasonable metrics for all systems.

Computational Details

Theoretical investigations were carried out using both density functional theory (DFT) and *ab initio* wavefunction theory (WFT) methods. The structures of complexes **1**–**5** (see Figure S1) were optimized by the B3LYP flavor of density functionals using the Stuttgart small-core (SSC) 1997 relativistic effective core potential and the associated basis sets for actinides and the Def2TZVPP basis sets for the light atoms.[61–63] The electronic absorption spectra of complexes **1**–**5** were calculated with scalar all-electron relativistic time-dependent DFT (TD-DFT) linear response theory based on the zeroth-order regular approximation (ZORA) Hamiltonian, as implemented in the Amsterdam Density Functional (ADF) suite of programs.[64] Two hundred excited states of the same spin multiplicity as the ground state were calculated for each complex. The conductor-like screening model (COSMO) was applied to investigate solvent effects for a dielectric constant (DC) ranging from 78 (water) down to 19 (pure HNO_3). The use of COSMO improved the calculated excitation energies; however, the differences between the results for DC between 78 and 19 were negligible. The latter are presented in this article. In order to assign the spectra, transitions of interest were analyzed in terms of donor—acceptor natural transition orbitals (NTO).[65]

WFT calculations were performed with a developer's version of the OpenMolcas package based on Molcas release 8.[66,67] The 2nd-order Douglas-Kroll-Hess scalar relativistic Hamiltonian[68] was employed in the calculations without Spin-orbit (SO) coupling, in conjunction with all-electron atomic natural orbital relativistically contracted basis sets (Np, Pu, Am = ANO-RCC-VTZP; N, O, H = ANO-RCC-VDZP). State-averaged CASSCF[69] (complete active space self-consistent field), with inclusion of dynamic electron correlation by 2nd order perturbation theory (CASPT2),[70] was employed. SO coupling was treated by state interaction among 'spin-free' (SF) CASSCF/PT2 wavefunctions, using the RASSI (restricted active space state interaction) program and atomic mean-field SO integrals. Note, each SF wavefunction has a well-defined spin multiplicity. For brevity, spin-free and spin-orbit CASSCF and CASPT2 calculation are in the following referred to as CAS-SF, CAS-SO, PT2-SF, and PT2-SO, respectively, which were used to calculate mainly the energies of low-energy electronic states arising from the 5f manifold. The active spaces spanned 10 orbitals, namely, the four nonbonding δ and ϕ An 5f orbitals, along with the An—O σ, $\sigma*$, π and $\pi*$ orbitals of the actinyl moieties, with between 7 and 10 electrons. Fourteen spin doublet states (7 ^2A_u and 7 ^2B_u roots) were calculated for $Np(VI)O_2(NO_3)_2 \cdot 2H_2O$, 60 spin-triplet states (30 ^3A_g and 30 ^3B_g roots) and 60 spin-singlet states (30 ^1A_g and 30 ^1B_g roots) for the Np(V) complex, 42 spin-triplet states (21 ^3A_g and 21 ^3B_g roots) and 42 spin-singlet states (21 ^1A_g and 21 ^1B_g roots) for the Pu(VI) complex, while spin quartet (35 ^4A_u and 35 ^4B_u roots) and doublet (35 ^2A_u and 35 ^2B_u roots) states were calculated for the Am(VI) complex. Visualizations of iso-surfaces of the DFT Kohn-Sham orbitals, NTOs, and natural orbitals[71] (NOs) of selected WFT spin states and SO states were created with the graphical user interface of ADF and the Exatomic suite.[72]

Results and Discussion:

Co-Crystallization of An(VI) or An(V) in UNH

Samples containing either a hexavalent (NpO_2^{2+}, PuO_2^{2+}, or AmO_2^{2+}) or pentavalent (NpO_2^+) TRU species were generated by crystallization of UNH in the presence of the oxidized TRU species, which resulted in a co-crystalized product, as described previously.[55] The hexavalent species, NpO_2^{2+}, PuO_2^{2+}, and AmO_2^{2+}, were removed from solution in near proportion to UO_2^{2+}, while the pentavalent species, NpO_2^+, was removed at a slightly less efficient manner (see Table 3). Both the near proportional removal of the hexavalent TRUs, AnO_2^{2+}, and the slightly less efficient removal of the pentavalent TRU, AnO_2^+—which is hindered by the charge balance requirements, forcing a defect in the lattice—indicate the actinyl species is being incorporated into the UO_2^{2+} positions within the lattice and will be discussed in detail later. This is not surprising, as the linear dioxo geometry is adopted by either valency of the actinyl cations, which allows for the local environment of the metal center to not experience any steric hinderance within the lattice. Moreover, scanning electron scanning electron microscopy coupled with energy dispersive X-ray spectroscopy (SEM-EDS) confirmed the homogeneous composition of all the materials containing TRUs, with similar distribution of U and the TRU species throughout the material (see Figure S4).

Table 3: UNH crystallization yields for the U and TRU species and ratios of the percent co-crystallization of U to TRUs.

TRU Species	% Crystallization U	TRU	Ratio U: TRU
U(VI)-only	89% ± 9%	-	
Np(VI)	96% ± 10%	91% ± 6%	1.0:0.94
Pu(VI)	86% ± 9%	78% ± 5%	1.0:0.92
Am(VI)	79% ± 8%	75% ± 5%	1.0:0.95
Np(V)	90% ± 9%	75% ± 5%	1.0:0.83

X-ray Absorption Fine Structure Spectroscopy

To understand the local environment of the An metal centers, L_3-edge EXAFS measurements were employed to directly probe the coordination environment of AnO_2^{2+} (An = Np, Pu, or Am) co-crystallized with UO_2^{2+} out of nitric acid. Consistent with previous EXAFS studies for Np and Am,[76,77] radiolytic degradation was observed for Np(VI), Pu(VI), and Am-containing solid-state samples, which limited the quality of the measured EXAFS data. The collection of EXAFS data for Np(V) was attempted, but due to low Np(V) concentrations (~ 3% w/w %) the signal-to-noise ratio was too low to obtain reliable results. Despite these limitations, we can still obtain quantitative information on the primary coordination structure of hexavalent ions and Am.

The experimental and fitted L_3 $k^3\chi(k)$ EXAFS data using the two-shell O_{ax},O_{eq} models for actinyl species and a single O shell for Am and real-space functions generated using the Fourier transforms are shown in Figure 1. It is apparent that the main EXAFS oscillations and the relative positions for the primary two peaks in the FT-EXAS are similar for U(VI), Np(VI), and Pu(VI). The main peak at ~1.3 Å (r + Δ) and the second peak at ~1.9 Å (r + Δ) correspond, respectively, to axial oxygens in the actinyl unit and O donor atoms of nitrates and water in the equatorial plane.[78–80] In contrast, a very different coordination is evident for Am, which shows a distinct $k^3\chi(k)$ oscillation pattern, with the main FT-EXAFS peak shifted to ~2.0 Å and only a small shoulder detectable at

~1.3 Å. As will be discussed in detail later, reduction of Am(VI) to Am(III) was observe over a period of weeks (see Figure S9) after the isolation of the samples, but prior to shipment to the APS. The shape and position of this peak is strikingly reminiscent of the FT-EXAFS spectrum of the Am nitrate complex published recently by Riddle *et al.*[76], where it was found based on UV-Vis spectroscopy that the initially prepared 50%:50% mixture of Am(V) and Am(III) species had reduced to Am(III) upon the return of samples from the synchrotron radiation facility. A distinguishable peak for U(VI) at ~3.6 Å (r + Δ) was previously[78–80] assigned to the enhanced multiple scattering involving U, N, and the distant O of the bidentate-coordinated nitrate anions. However, this peak is not resolved for Np(VI), Pu(VI), and Am-containing samples having rather noisy spectra.
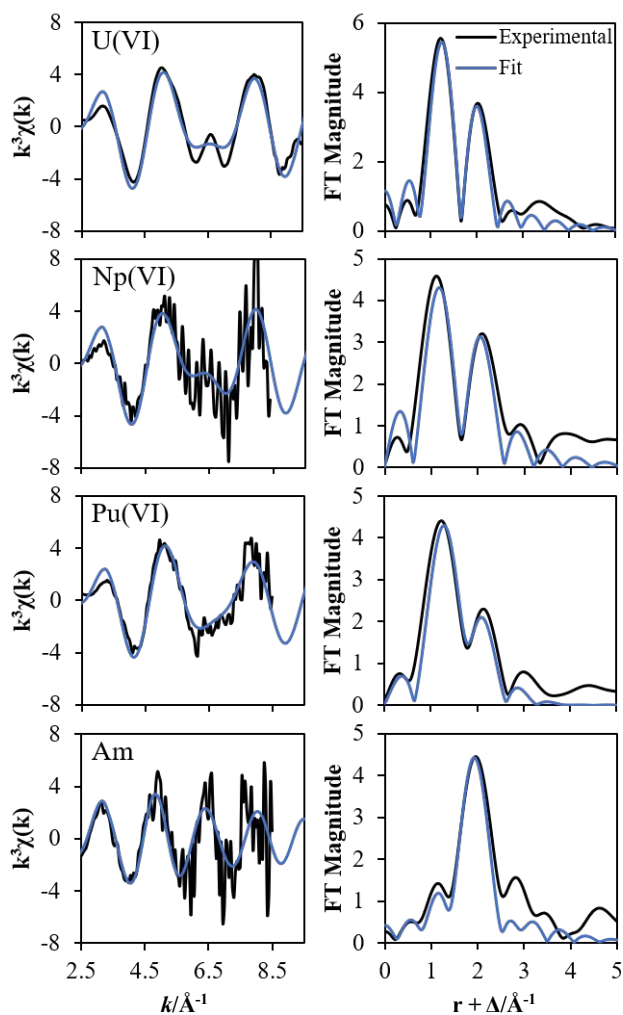

Figure 1. L3-edge $k^3\chi(k)$ EXAFS data (left) and the corresponding Fourier transforms (right) of the U(VI), Np(VI), Pu(VI), and Am co-crystallized samples (top to bottom, respectively). Experimental data in black and fit in blue. The upper limit of $k^3\chi(k)$ is shown up to the fitting range, which is 9.5 Å^{-1} for U(VI) and 8.5 Å^{-1} for the other samples.

Fitting parameters accounting for the major EXAFS features due to backscattering from the first-coordination shell are summarized in Table 4. Despite the limited *k*-range for these systems, resulting in relatively large uncertainties of the fitting parameters, the employed models provide

8

good fits to the EXAFS data with physically reasonable optimized metrics. The differences in the average bond distances for the axial and equatorial O atoms between EXAFS and DFT or diffraction data[74,77,80–83] are all within the uncertainty of EXAFS results. It is not unexpected to have a larger Debye-Waller factor (σ^2) for O_{eq} atoms of water and nitrate with various similar distances. Similar metrical parameters for UO_2^{2+}, NpO_2^{2+}, and PuO_2^{2+} strongly suggest that they are all similarly coordinated in the solid state and, thus, expected to be randomly incorporated into the UNH crystal lattice, occupying the UO_2^{2+} positions. A single O shell model was employed to fit the main peak in the FT-EXAFS spectrum of a reduced Am sample. The average bond distance for the near-neighbor O atoms is 2.48 Å, which coincides with previously reported[76] value for the reduced Am(V) to Am(III) sample and within a range of 2.46–2.58 Å Am–O bond distances in the $[Am^{III}(H_2O)_9](CF_3SO_3)_3$ crystal structure.[83]

Table 4. Metrics from the EXAFS data fitting using the two-shell O_{ax}, O_{eq} models for actinyl species and a single O shell for Am, along with the comparison of interatomic distances from DFT calculations and XRD data[a]

Element	Atom	CN	EXAFS R/Å	σ^2x10³/Å²	$\Delta E(0)$/eV	DFT[b]	ND[c],XRD[d]
U	O_{ax}	2	1.75(2)	0.0015(13)	8.3(25)	1.762	1.761, 1.742
	Q_{eq}	6	2.46(3)	0.0094(20)		2.508	2.483, 2.480
Np	O_{ax}	2	1.75(4)	0.0018(31)	7.9(57)	1.742	1.744
	Q_{eq}	6	2.50(6)	0.0078(41)		2.498	2.477
Pu	O_{ax}	2	1.76(3)	0.0016(20)	9.9(51)	1.732	1.728
	Q_{eq}	6	2.45(7)	0.0126(40)		2.489	2.475
Am	O	10	2.48(3)	0.0096(24)	8.2(19)	-	2.503

[a]The amplitude reduction factor $S_0^2 = 0.92$ and the coordination numbers (CN) were fixed during the fitting. [b]DFT calculations were performed at the B3LYP/SSC(Ac)/ Def2TZVPP level. [c]The average distances from neutron diffraction (ND) analysis that appear first are for $[UO_2(NO_3)_2(H_2O)_2]\cdot4H_2O$.[74] [d]The X-ray diffraction distances are for the isostructural $[AcO_2(NO_3)_2(H_2O)_2]\cdot H_2O$ (Ac = U, Np, and Pu)[80–82] and $[Am^{III}(H_2O)_9](CF_3SO_3)_3$.[83]

The position of the L_3 absorption edge energy in the X-ray absorption near edge structure (XANES) spectrum can give independent information about the oxidation state of an Am sample. The tabulated value of the edge energy for the trivalent AmF_3 and $Cs_2NaAmCl_6$ standards determined from the maximum in the first derivative is 18511 eV,[84] which is 7 eV lower than the value of 18504 eV for the Am metal[85] and 4 eV higher than the value of 18515 eV for presumably tetravalent Am in $Pb_2Sr_2AmCu_3O_8$.[84] Using Nb metal as an internal standard, the edge energy for the Am-containing sample is 18510.5 eV. This matches well with the tabulated value for the trivalent Am standards.[84] We therefore conclude from the L_3 absorption edge that the Am(VI) sample has reduced to Am(III), which is fully consistent with the EXAFS analyses, as well as the UV-Vis-NIR analysis, which will be discussed next.

Diffuse Reflectance UV-Vis-NIR Spectroscopy:

As was mentioned earlier, the features in the diffuse reflectance UV-Vis-NIR absorption spectra of the crystalline phases resulting from the co-crystallization of oxidized TRUs with UNH were reported in a previous contribution, however, the transitions have so far not been assigned.[55] An in-depth evaluation utilizing TDDFT calculations to make these assignments is presented next. Based on the results obtained from EXAFS analysis, as discussed previously, the dinitrate species, $AnO_2(NO_3)_2\cdot2H_2O$, was selected for these studies. To get a detailed description of the ground and low-energy excited states of the complexes with unpaired electrons, WFT calculations with SO

coupling were performed additionally. A qualitative molecular orbital scheme for $AnO_2(NO_3)_2 \cdot 2H_2O$ is depicted in Figure 2. The spectroscopically relevant MOs are listed in Tables S2 to S6. The ground-state structures of $AnO_2(NO_3)_2 \cdot 2H_2O$ were determined to have C_{2h} symmetry. As far as the actinyl moieties are concerned, as in the free actinyl species[71,86], there are occupied *ungerade* bonding 5f σ and π orbitals, with their unoccupied correlating antibonding counterparts, displaying strong An 5f-O_{yl} 2p orbital mixing. The four nonbonding 5f orbitals, labeled according to the (quasi-) linear symmetry of the actinyl ions as 5f δ and ϕ, are split energetically in the presence of the equatorial (eq) ligands. Some of these formally nonbonding 5f orbitals exhibit slight antibonding character with respect to the equatorial O ligands. This means there are occupied ligand-centered bonding counterparts at lower energy, arising from (relatively weak) ligand to metal donation bonding in the equatorial plane. Likewise, there is donation bonding involving the metal 6d shell. The energetic ordering and the compositions of selected MOs are provided in the SI.
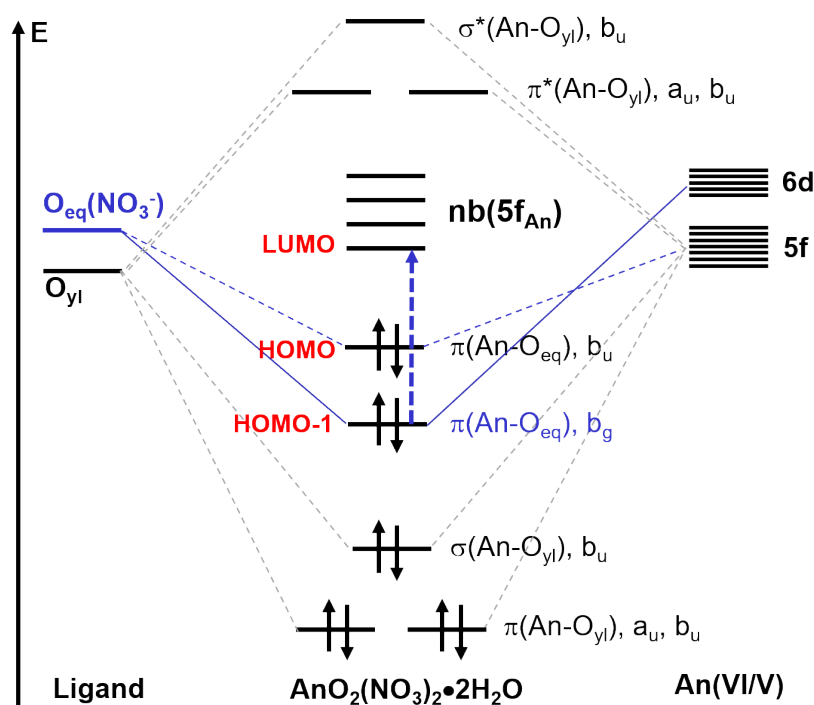

Figure 2. Qualitative molecular orbital diagram scheme for two ligands (O_{yl}, O_{eq}) and An(VI/V) on the left and right sides, respectively. The vertical dashed arrows (blue color) indicate the spin allowed ligand-to-metal charge transfer (LMCT) excitation. The varying occupations of the nonbonding 5f orbitals of $AnO_2(NO_3)_2 \cdot 2H_2O$ are not indicated by arrows.

To begin with, the diffuse reflectance absorption spectrum of the UNH crystalline phase resulting from the crystallization of the U(VI)-only system, shown in Figure S5, is relatively simple. The U(VI) characteristic strong absorbance in the range 375–485 nm was present in the solid state and had a λ_{max} of 418 nm (2.97 eV), with another relatively intense absorption at 426 nm (2.91 eV). According to the natural transition orbital (NTO) analysis of $UO_2(NO_3)_2 \cdot 2H_2O$, shown in Table 5, the observed absorption features assigned primarily as ligand-to-metal charge transfer (LMCT). The predicted allowed transitions match the observed spectrum well. The two main transitions are from HOMO-1 to a nonbonding orbital (LUMO or LUMO+2). The corresponding energies are 2.95 eV (420 nm) and 2.82 eV (440 nm). The deviations between the theoretical and experimental

wavelengths are minor, for this and the other complexes, and within the expected error ranges for these types of calculations.

Table 5. Natural transition orbital (NTO) analysis for $UO_2(NO_3)_2 \cdot 2H_2O$ in the ~375–485 nm spectral region. Orbital isosurface values are ± 0.03.

LMCT	f	Donor NTO	Acceptor NTO	Weight
2.82 eV (HOMO-1$\rightarrow$ LUMO)	0.0037			100%
2.89 eV (HOMO-1$\rightarrow$ LUMO+1)	0.0001			100%
2.95 eV (HOMO-1$\rightarrow$ LUMO+2)	0.0012			100%

Next the system which incorporated Np(VI) into the UNH crystalline phase was examined. Figure S6 displays the optical spectrum of Np(VI). The major features are a broad band ranging from 520 to 590 nm with λ_{max} at 559 nm (2.22 eV), a small band at 624 nm (1.99 eV) and a band at 1089 nm (1.14 eV). According to the NTO analysis of $NpO_2(NO_3)_2 \cdot 2H_2O$, the higher energy transition at 528 nm (2.35 eV) is a LMCT involving HOMO-2 and LUMO+1, as shown in Table S7, and it matches the experimental absorption region (520–590 nm). Another transition (calc. 608 nm, 2.04 eV) is characterized as LMCT involving HOMO-2 to LUMO. Meredith et $al.$[87] observed a signal in the range of 500 to 600 nm for Np doped torbernite/meta-torbernite crystals which was attributed to characteristic Np(VI) transitions. In those studies, the Np(VI) metal center was a square bipyramidal coordination, while in the current work, the Np(VI) coordination is hexagonal bipyramidal. The lower energy transition at 1089 nm (1.14 eV) is an f-f transition, which results in its low intensity. The calculated electric dipole oscillator strengths for the 5f-5f transitions for all complexes are effectively zero. The observed, albeit low, intensity indicates that the Np(VI) incorporated UNH-phase either possesses some higher level of structural anisotropy than the optimized structures of the isolated complexes, or the intensity is vibronic or magnetic.

For a more accurate description of the electronic states of the 5f manifold, we turned to WFT calculations where the effects of SO coupling (SOC) are taken into consideration. The spin ground state (GS) of $NpO_2(NO_3)_2 \cdot 2H_2O$ is a doublet (1^2A_u) in which the unpaired electron populates the 5f ϕ orbital of the neptunyl moiety. In contrast, the CAS-SO GS has 57% contribution from 1^2A_u, and 27% contribution from the low-lying state 2^2B_u along with a small admixture from state 1^2B_u, as shown in Table S9. The Natural orbitals (NOs) and occupation numbers of the CAS-SF and CAS-SO ground state are shown in Figure 3. The effects of SOC can be clearly seen from the NOs,

as shown by the changes in the occupation numbers. It may seem counterintuitive that the SOC leads to an increase of the occupation of the more strongly antibonding 5f ϕ orbital. However, the mixing of the spin GS with excited spin state components, which leads to the changes in the NO occupation, comes with a stabilizing contribution from the SO interaction in the total energy. The low-energy electronic excitation energy (calc. 1.15 eV, 1078 nm) from the CASSCF calculation reproduces the experiment (1.14 eV, 1089 nm) well and confirms that the observed weak band is due to an f-f transition.
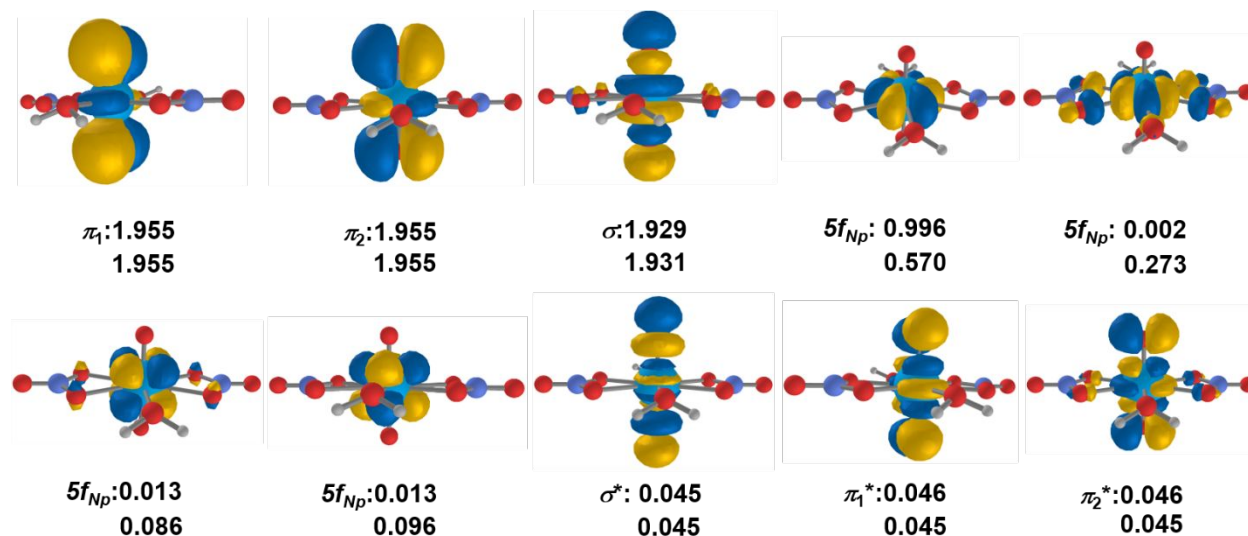

π_1:1.955 π_2:1.955 σ:1.929 $5f_{Np}$: 0.996 $5f_{Np}$: 0.002
1.955   1.955   1.931   0.570   0.273

$5f_{Np}$:0.013 $5f_{Np}$:0.013 σ^*: 0.045 π_1^*:0.046 π_2^*:0.046
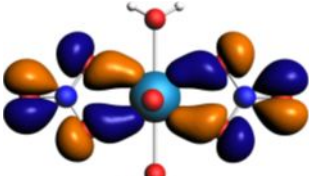0.086   0.096   0.045   0.045   0.045
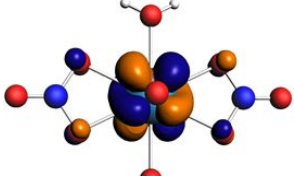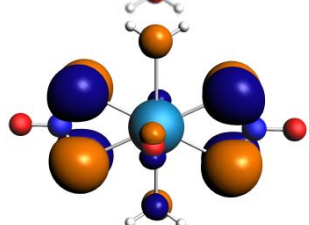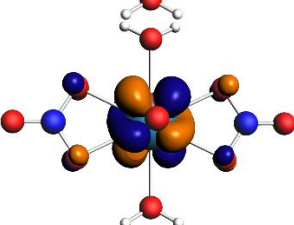
Figure 3. Natural orbitals (NOs) and occupation numbers of the CAS-SF (upper set of occupation numbers) and CAS-SO (lower set of numbers) ground state of $NpO_2(NO_3)_2 \cdot 2H_2O$.

The Pu(VI)-incorporated system was examined next (see Figure S7). The absorption spectrum of Pu(VI) is more complex than the spectrum for Np(VI), containing more transitions in the UV-Vis-NIR region. First, Pu(VI) exhibits several features with a broad band beginning around 500 nm and extending up to 580 nm, with distinct absorbances at 528 nm (2.36 eV), 538 nm (2.31 eV), and 556 nm (2.23 eV). The GS of $PuO_2(NO_3)_2 \cdot 2H_2O$ has two unpaired electrons in the four nonbonding orbitals, leading to a triplet spin GS. As seen from Table S4, HOMO and HOMO-1 of the Pu(VI) complex represent the two occupied nonbonding spin orbitals, which are close in energy. HOMO-2 has stronger orbital overlap of Pu 5f with O_{eq} than the corresponding orbitals of U(VI) and Np(VI). The energy gap between HOMO and LUMO is around 0.43 eV. Based on the NTO analysis of $PuO_2(NO_3)_2 \cdot 2H_2O$ (Table 6), the excitation from HOMO-4 to LUMO gives the transition at 537 nm (2.31 eV), which agrees with the experimental observation in the range 500–580 nm. Note that HOMO-4 is a linear combination of nitrate oxygen lone pairs (LPs), while LUMO is metal-centered, giving the assignment of the transition as LMCT. The other major band extends from 775 nm to 850 nm, with four distinct signals at 797 nm (1.56 eV), 801 nm (1.55 eV), 808 nm (1.53 eV), and 812 nm (1.53 eV), and a shoulder at 818 nm (1.52 eV). These excitations are attributed to LMCT involving HOMO-3 and LUMO, with HOMO-3 being another ligand-centered π orbital with predominant contributions from O_{eq} LPs. Gaunt et al.[81] observed similar bands upon crystallization of $PuO_2(NO_3)_2 \cdot 3H_2O$ out of concentrated HNO_3, but did not attempt to assign the transitions. The NTO analysis produces several transitions with energies in relatively good agreement of those observed experimentally. There are also f-f transitions with low or no

12

oscillator strength, as described later. As was previously mentioned, the presence of f-f intensity could be an indication that the symmetry of the system is being reduced by some mechanism, or the intensity is vibronic or magnetic.

Table 6. Natural transition orbital (NTO) analysis for $PuO_2(NO_3)_2 \cdot 2H_2O$ in the ~500-580 nm and ~ 775-850 nm absorption spectral region. Orbital isosurface values are ±0.03.

LMCT	f	Donor NTO	Acceptor NTO	Weight
1.53 eV (HOMO-3→ LUMO)	0.0004			100%
2.31 eV (HOMO-4→ LUMO)	0.0085			98%

For the WFT calculations, the f^n (n≥2) systems require treating the dynamic correlation.[88–90] Therefore, we discuss the PT2 data. As shown in Table S10, the spin GS of $PuO_2(NO_3)_2 \cdot 2H_2O$ is a triplet (1^3B_g), determined by two unpaired electrons populating the 5f ϕ and 5f δ orbitals essentially as in the free plutonyl ion. The combination of SOC and the equatorial ligand field causes the SO GS to be a mixture of 1^3B_g (46%) and 1^3A_g (46%) spin states, along with a minor contribution from the singlet state 1^1B_g. The NOs of the spin GS and the ground SO states are shown in Figure S2. Calculated PT2-SO transition energies of the Pu(VI) complex correlate with the features observed experimentally in the bands of 900–960 nm and 1120–1300 nm, respectively. The corresponding calculated excitation wavelengths (energies) are 876 nm (1.42 eV) and 1278 nm (0.97 eV). The former excitation energy is overestimated relative to the corresponding experimental absorption region at 900-960 nm. It is possible that PT2 is over-correcting the excitation energy calculated at the CAS-SO level, which is 1.28 eV (968 nm) and therefore somewhat too low. In any case, the deviations from the experimentally observed absorption range are within the uncertainties of the computational model, and not large. The WFT calculations therefore assign the observed weak bands to f-f transitions.

Following Np(VI) and Pu(VI), which are both easily produced and stabilized in solution, focus was placed on incorporation of Am(VI) in the UNH crystalline phase. As mentioned earlier, Am(VI) requires a highly oxidizing environment (Am(III)/Am(VI) ~ +1.7 V vs NHE[54]) and readily reacts with reducing agents including organic materials, the surface of plastics, and various radiolysis products, which often results in the presences of multiple oxidation states. This was the case during Am(VI) co-crystallization with UNH, where the majority, approximately 78%, was present as Am(VI), but small amounts of both Am(III) and Am(V), roughly 10% and 12%, respectively, also persisted in solution (see Figure S8). At first glance, the crystalline phase also appeared to contain multiple species, but upon closer examination, most of the absorption wavelengths remain completely unchanged between the crystalline sample and that of the solution. As will be discussed later, these unchanged signals are assumed to be from Am dissolved in

13

residual mother liquor droplets adhered to the surface of the solid, rather than from Am incorporated into the UNH phase. This is supported by the fact that the U(VI) signal more closely resembles the solution phase, as opposed to what was observed in the UNH crystals (see Figure S5). There is, however, a new band at 955 nm (1.30 eV) in the crystalline phase, which, as will be discussed in a moment, can be assigned to Am(VI).

To assess if surface adsorption of the mother liquor had occurred, resulting in the presence of the unchanged signals from Am(III), Am(V), and Am(VI), a second spectrum of the crystalline phase was obtained 10 d after crystallization (8 d after the first spectrum). This provided ample time for the Am(VI) in the adsorbed mother liquor film to reduce to Am(III), and in fact the band at 996 nm completely disappears, while the 504 nm and 814 nm bands increase relative to the U(VI) by approximately 10%, as shown in Figure S9. A portion of the crystalline phase was then washed with an 8 M HNO_3 solution containing 1.9 M U(VI), which resulted in a 70% decrease in the Am(III) signal compared to that of U(VI), while the broad, low intensity absorbance in the region of 590–680 nm and the signal at 955 nm, both assumed to arise from Am(VI), remained constant relative to U(VI). It should be noted, the structure of the U(VI) signal changed upon washing to be in line with the UNH crystalline product (see inset of Figure S9). This further indicates the mother liquor film was present prior to washing and was then removed during the washing process.

Before assigning the spectrum, it is helpful to examine the electronic structure of $AmO_2(NO_3)_2 \cdot 2H_2O$. The ground spin state of the Am (VI) complex is a quartet with three unpaired electrons in the nonbonding spin orbitals HOMO-2 to HOMO. As we see from Table S5, these three highest occupied orbitals are primarily Am 5f, with similar energy. The LUMO has 70% weight from Am 5f and 26% O 2p. LUMO+1 and LUMO+2 are near-degenerate axial dioxo antibonding π^* orbitals with about 56% Am 5f and 36% O_{yl} weights. The energy gap between the HOMO (singly-occupied) and LUMO is 1.36 eV. HOMO-3 is a ligand-centered π bonding orbital with some admixture from Am 6d. According to the NTO analysis (see Table S8), the excitations from HOMO-3 to LUMO and LUMO+1 give two excited states, at 2.02 eV (614 nm) and 2.57 eV (482 nm). The former matches well with the experimentally recorded absorption in the region of 590–680 nm. The calculated excitation wavelength involving HOMO-3 to LUMO+1 at 482 nm (2.57 eV) is slightly below the experiment absorption region (504 nm, 2.46 eV). However, the discrepancy is well within the expected computational error bars. The lower energy transition at 955 nm is discussed in the next paragraph.

Results from the WFT calculations for the Am (VI) complex are summarized in Table S11. The PT2-SO GS has 46% contribution (weight) from 1^4B_u, and 22% contribution from the low-lying state 1^4A_u along with small admixtures of 2^4A_u and 2^4B_u. The NOs and occupation numbers of the ground state and the sixth excited state are shown in Figure 4. As a result of SOC, the combined occupation of 5f ϕ increases at the expense of the Am 5f δ occupation, and there is a large shift of electron density, about 0.3 electrons, from the nonbonding to the mildly antibonding 5f ϕ. The theoretical transition energy (912 nm, 1.36 eV) assigned to correspond to the observed transition at 955 nm (λ_{max}, 1.30 eV) results from the sixth excited PT2-SO state. Examining the NOs and occupation number of the GS and sixth excited state (see Figure 4), attributed to the new absorbance, it can be seen that an electron is promoted primarily from the Am centered pair of 5f δ orbitals to the near-degenerate Am-O_{yl} π^* anti-bonding orbitals. The target orbitals have substantial Am 5f character, and therefore the transition has partial f-f character. At this point, the

14

root cause of the reduction in symmetry about the Am(VI) metal center is not clear, but the observation of forbidden transitions experimentally, indicates some level of anisotropy. As mentioned previously, vibronic or magnetic intensity may also be present.
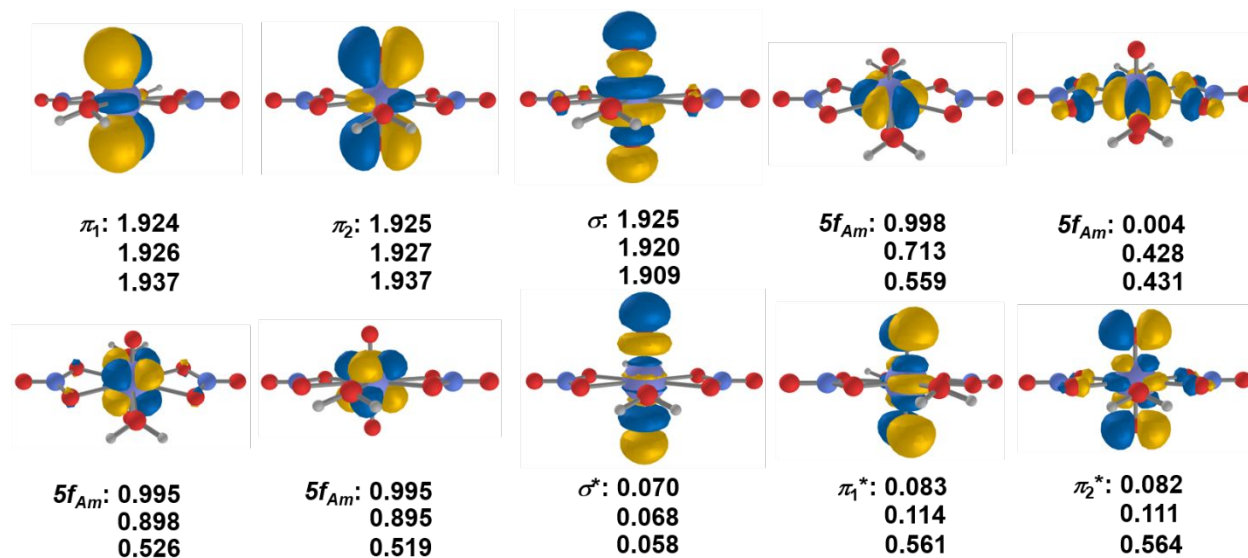

Figure 4. Natural orbitals (NOs) and occupation numbers of the PT2-SF ground state (upper rows of data), PT2-SO (middle) ground state, and PT2-SO sixth excited state (lower rows of data) of $AmO_2(NO_3)_2 \cdot 2H_2O$.

Lastly, the incorporation of Np(V) into the UNH-phase was examined. While steric considerations required for co-crystallization are met by the linear dioxo geometrical configuration, maintaining charge balance upon co-crystallization of the singly charged NpO_2^+ molecular cation necessitates defects be introduced in to the lattice. The introduction of defects should reduce the efficiency of including the Np(V) into the lattice, which is, in fact, what was observed, with slightly less efficient Np(V) incorporation into the UNH-phase over the other An(VI) species (see Table 3). Nonetheless, spectroscopic investigation of the crystalline product revealed spectral features assigned to Np(V) (see Figure S10). The narrow band at 995 nm (1.25 eV) can be attributed to a 5f-5f excitation of Np(V).

To interpret the observed spectrum, it is necessary to understand the electronic structure of the Np(V) complex. Compared with Np(VI), the GS of $NpO_2(NO_3)_2^- \cdot 2H_2O$ has one more unpaired electron populating the nonbonding orbital, i.e. $5f^2$, resulting in a spin-triplet state. This is expected, because Np(V) and Pu(VI) have the same number of unpaired electrons. As shown in Table S1, the $Np(V)-O_{yl}$ and $Np(V)-O_{eq}$ distances are elongated by 0.06/0.07 and 0.14 Å, respectively, relative to the Np(VI)/Pu(VI) complex. The π bonding orbital representing the interaction of Np with the O_{eq} ligand orbitals has 6% Np 5f weight in the Np(V) complex, whereas the weight is 13% for the Np(VI) complex, and 17% for the Pu(VI) complex. This shows that the elongated distances go along with a weakened equatorial donation bonding. In other words, the equatorial donation bonding is the strongest for Pu(VI), weaker when going to Np(VI), and much weaker for Np(V). The Pu vs. Np covalency trend echoes that for the An-O_{yl} bonds.[86] According to the NTO analysis of $NpO_2(NO_3)_2^- \cdot 2H_2O$ (see Table 7), the transitions calculated at 861 nm (1.44 eV) and 918 nm (1.35 eV) are assigned as metal-to-ligand charge transfer (MLCT) involving

Physical Chemistry Chemical Physics

HOMO-1 and HOMO to LUMO+2. The calculated wavelengths agree with the experimental absorption region from 760 nm to 920 nm.

Table 7. Natural transition orbital (NTO) analysis for Np(V)O$_2$(NO$_3$)$_2^-$·2H$_2$O in the ~760–920 nm absorption spectral region. Orbital isosurface values are ±0.03.

MLCT	f	Donor NTO	Acceptor NTO	Weight
1.35 eV (HOMO→ LUMO+2)	0.00001			100%
1.44 eV (HOMO-1→ LUMO+2)	0.0078			100%

For assigning the f-f transitions, PT2 WFT calculations were performed. The results are shown in Table S12. For the NpO$_2$(NO$_3$)$_2^-$·2H$_2$O complex, the PT2-SO GS has 45% contribution from 1^{3}B$_g$, and an equivalent weight from the low-lying state (1^{3}A$_g$) along with minor contribution from the singlet state 1^{1}B$_g$. Calculated SO transition energies (1.22 eV, 1016 nm) of the Np(V) complex match closely the features observed in the experimental absorption spectrum (λ_{max}, 995 nm, 1.25 eV). As stated before, this type of 5f-5f transition exhibits very weak and low intensity.

Conclusions:

In conclusion, the spectroscopic characterization of crystalline solids resulting from the crystallization of UNH in the presence of Np(VI), Pu(VI), Am(VI), or Np(V) out of HNO$_3$ systems has been conducted via DR UV-Vis-NIR, SEM-EDS, and EXAFS, which provides strong evidence that the TRU species are incorporated in the lattice, occupying the U(VI) position. Density functional and multi-reference wavefunction calculations were used to assign the transitions observed in the solid-state absorption spectra. In the first step, we determined the electronic structure and chemical bonding of An(VI/V)(NO$_3$)$_2$·2H$_2$O complexes by performing DFT calculations. There are equatorial ligand-centered orbitals that exhibit donation bonding into the An 5f and 6d shells. These orbitals participate in the LMCT transitions assigned in the spectra of the U(VI), Np(VI), Pu(VI), and Am(VI) complexes, with the acceptor orbitals being formally non-bonding An 5f, according to NTO analyses of the TDDFT calculations. In contrast, the Np(V) complex shows MLCT in the region 760-920 nm. The wavefunction calculations include SO coupling and therefore give an accurate description of the ground state and low-energy excited states from the 5f manifold. Based on the wavefunction calculations, most of the observed long-wavelength / low energy absorption bands with weak intensity for the TRU complexes are assigned to 5f-5f transitions. For the Am(VI) complex, a newly observed absorption band is assigned to a transition from 5f$_\delta$ to Am-O$_{yl}$ π^*. The accompanying NO analysis gives an intuitive description of the complicated electronic states, such that the admixture of different spin states under the SO interaction, or an electronic excitation, are reflected by corresponding changes in the occupations. We stress that this NO description does not imply further approximations in the calculations.

Rather, it condenses the enormous complexity of the many-electron SO-coupled wavefunctions into chemically intuitive pictures. Application of these approaches will continue to broaden our understanding of more complicated actinide compounds.

The calculations confirm the dinitrate species, $An(VI/V)(NO_3)_2 \cdot 2H_2O$, with similar coordination is present for all five metal centers. This was in line with the EXAFS data, with the exception of Am, which reduced to Am(III) prior to the beamline experiment. The co-crystallization of the oxidized TRUs—the penta- and hexavalent species—with UNH, represents a significant advance from not only a practical standpoint in providing an elegant solution for UNF recycle, but also as an avenue to expand the fundamental understanding of the 5f electron behavior in the solid-state.

■AUTHOR INFORMATION
Corresponding Authors
*burns.jon@tamu.edu
*jochena@buffalo.edu

ORCID
Xiaojuan Yu: 0000-0001-9412-6170
Jeffrey D. Einkauf: 0000-0002-6403-4301
Vyacheslav S. Bryantsev: 0000-0002-6501-6594
Michael C. Cheshire: 0000-0003-1792-6881
Benjamin J. Reinhart: 0000-0001-5654-8823
Jochen Autschbach: 0000-0001-9392-877X
Jonathan D. Burns: 0000-0003-0301-9607

Present Addresses
†Chevron Technology Center, 3901 Briarpark Drive, Houston, TX 77042, USA.

Author Contributions
§X. Yu and J. D. Einkauf contributed equally to this work.

Notes
The authors declare no competing financial interest.

Reference:

1   J. K. Pagano, J. Xie, K. A. Erickson, S. K. Cope, B. L. Scott, R. Wu, R. Waterman, D. E. Morris, P. Yang, L. Gagliardi and J. L. Kiplinger, Actinide 2-metallabiphenylenes that satisfy Hückel's rule, *Nature*, 2020, **578**, 563–567.

2   J. Autschbach, Orbitals for Analyzing Bonding and Magnetism of Heavy-Metal Complexes, *Comments Inorg. Chem.*, 2016, **36**, 215–244.

3   M. S. Dutkiewicz, J. H. Farnaby, C. Apostolidis, E. Colineau, O. Walter, N. Magnani, M. G. Gardiner, J. B. Love, N. Kaltsoyannis, R. Caciuffo and P. L. Arnold, Organometallic neptunium(III) complexes, *Nat. Chem.*, 2016, **8**, 797–802.

4   M. G. Ferrier, E. R. Batista, J. M. Berg, E. R. Birnbaum, J. N. Cross, J. W. Engle, H. S. La Pierre, S. A. Kozimor, J. S. Lezama Pacheco, B. W. Stein, S. C. E. Stieber and J. J. Wilson, Spectroscopic and computational investigation of actinium coordination chemistry, *Nat. Commun.*, 2016, **7**, 12312.

5   L. Zhang, G. Hou, G. Zi, W. Ding and M. D. Walter, Influence of the 5f Orbitals on the Bonding and Reactivity in Organoactinides: Experimental and Computational Studies on a Uranium Metallacyclopropene, *J. Am. Chem. Soc.*, 2016, **138**, 5130–5142.

6   D. E. Smiles, G. Wu, P. Hrobárik and T. W. Hayton, Use of 77 Se and 125 Te NMR Spectroscopy to Probe Covalency of the Actinide-Chalcogen Bonding in [Th(E n){N(SiMe 3) 2 } 3] − (E = Se, Te; n = 1, 2) and Their Oxo-Uranium(VI) Congeners, *J. Am. Chem. Soc.*, 2016, **138**, 814–825.

7   S. K. Cary, M. Vasiliu, R. E. Baumbach, J. T. Stritzinger, T. D. Green, K. Diefenbach, J. N. Cross, K. L. Knappenberger, G. Liu, M. A. Silver, A. E. DePrince, M. J. Polinski, S. M. Van Cleve, J. H. House, N. Kikugawa, A. Gallagher, A. A. Arico, D. A. Dixon and T. E. Albrecht-Schmitt, Emergence of californium as the second transitional element in the actinide series, *Nat. Commun.*, 2015, **6**, 6827.

8   M. J. Polinski, E. B. Garner, R. Maurice, N. Planas, J. T. Stritzinger, T. G. Parker, J. N. Cross, T. D. Green, E. V. Alekseev, S. M. Van Cleve, W. Depmeier, L. Gagliardi, M. Shatruk, K. L. Knappenberger, G. Liu, S. Skanthakumar, L. Soderholm, D. A. Dixon and T. E. Albrecht-Schmitt, Unusual structure, bonding and properties in a californium borate, *Nat. Chem.*, 2014, **6**, 387–392.

9   S. G. Minasian, J. M. Keith, E. R. Batista, K. S. Boland, D. L. Clark, S. A. Kozimor, R. L. Martin, D. K. Shuh and T. Tyliszczak, New evidence for 5f covalency in actinocenes determined from carbon K-edge XAS and electronic structure theory, *Chem. Sci.*, 2014, **5**, 351–359.

10   C. J. Burns, CHEMISTRY: Bridging a Gap in Actinide Chemistry, *Science*, 2005, **309**,

1823–1824.

11   A. P. Sattelberger and M. J. A. Johnson, Uncovering the Uranium-Nitrogen Triple Bond, *Science*, 2012, **337**, 652–653.

12   L. Gagliardi and B. O. Roos, Quantum chemical calculations show that the uranium molecule U2 has a quintuple bond, *Nature*, 2005, **433**, 848–851.

13   E. Lu, S. Sajjad, V. E. J. Berryman, A. J. Wooles, N. Kaltsoyannis and S. T. Liddle, Emergence of the structure-directing role of f-orbital overlap-driven covalency, *Nat. Commun.*, 2019, **10**, 634.

14   W. J. Evans, Molecular Octa-Uranium Rings with Alternating Nitride and Azide Bridges, *Science*, 2005, **309**, 1835–1838.

15   D. M. King, F. Tuna, E. J. L. McInnes, J. McMaster, W. Lewis, A. J. Blake and S. T. Liddle, Synthesis and Structure of a Terminal Uranium Nitride Complex, *Science*, 2012, **337**, 717–720.

16   T. W. Hayton, An actinide milestone, *Nat. Chem.*, 2013, **5**, 451–452.

17   T. W. Hayton, Synthesis of Imido Analogs of the Uranyl Ion, *Science*, 2005, **310**, 1941–1943.

18   E. Lu, B. E. Atkinson, A. J. Wooles, J. T. Boronski, L. R. Doyle, F. Tuna, J. D. Cryer, P. J. Cobb, I. J. Vitorica-Yrezabal, G. F. S. Whitehead, N. Kaltsoyannis and S. T. Liddle, Back-bonding between an electron-poor, high-oxidation-state metal and poor π-acceptor ligand in a uranium(v)–dinitrogen complex, *Nat. Chem.*, 2019, **11**, 806–811.

19   J. Du, C. Alvarez-Lamsfus, E. P. Wildman, A. J. Wooles, L. Maron and S. T. Liddle, Thorium-nitrogen multiple bonds provide evidence for pushing-from-below for early actinides, *Nat. Commun.*, 2019, **10**, 4203.

20   E. Epifano, M. Naji, D. Manara, A. C. Scheinost, C. Hennig, J. Lechelle, R. J. M. Konings, C. Guéneau, D. Prieur, T. Vitova, K. Dardenne, J. Rothe and P. M. Martin, Extreme multi-valence states in mixed actinide oxides, *Commun. Chem.*, 2019, **2**, 59.

21   M. P. Kelley, I. A. Popov, J. Jung, E. R. Batista and P. Yang, δ and φ back-donation in AnIV metallacycles, *Nat. Commun.*, 2020, **11**, 1558.

22   J. N. Cross, J. Su, E. R. Batista, S. K. Cary, W. J. Evans, S. A. Kozimor, V. Mocko, B. L. Scott, B. W. Stein, C. J. Windorff and P. Yang, Covalency in Americium(III) Hexachloride, *J. Am. Chem. Soc.*, 2017, **139**, 8667–8677.

23   T. Vitova, I. Pidchenko, D. Fellhauer, P. S. Bagus, Y. Joly, T. Pruessmann, S. Bahl, E. Gonzalez-Robles, J. Rothe, M. Altmaier, M. A. Denecke and H. Geckeis, The role of the 5f valence orbitals of early actinides in chemical bonding, *Nat. Commun.*, 2017, **8**, 16053.

24   N. S. Settineri, M. E. Garner and J. Arnold, A Thorium Chalcogenolate Series Generated by Atom Insertion into Thorium–Carbon Bonds, *J. Am. Chem. Soc.*, 2017, **139**, 6261–6269.

25   R. W. Grimes and W. J. Nuttall, Generating the Option of a Two-Stage Nuclear Renaissance, *Science*, 2010, **329**, 799–803.

26   W. C. Sailor, NUCLEAR POWER:A Nuclear Solution to Climate Change?, *Science*, 2000, **288**, 1177–1178.

27   P. A. Kharecha and J. E. Hansen, Prevented mortality and greenhouse gas emissions from historical and projected nuclear power., *Environ. Sci. Technol.*, 2013, **47**, 4889–95.

28   S. Tachimori and Y. Morita, in *Ion Exchange and Solvent Extraction A Series of Advances, Volume 19*, ed. B. A. Moyer, CRC Press, Philadelphia, 2009, pp. 1–63.

29   C. Poinssot, B. Boullis and S. Bourg, in *Reprocessing and Recycling of Spent Nuclear*

          Fuel, ed. R. Taylor, Elsevier, Cambridge, 2015, pp. 27–48.

30   M. Salvatores and G. Palmiotti, Radioactive waste partitioning and transmutation within advanced fuel cycles: Achievements and challenges, *Prog. Part. Nucl. Phys.*, 2011, **66**, 144–166.

31   R. A. Wigeland, T. H. Bauer, T. H. Fanning and E. E. Morris, Separations and Transmutation Criteria to Improve Utilization of a Geologic Repository, *Nucl. Technol.*, 2006, **154**, 95–106.

32   T. A. Todd and R. A. Wigeland, in *Separations for the Nuclear Fuel Cycle in the 21 st Century*, eds. G. J. Lumetta, K. L. Nash, S. B. Clark and J. I. Friese, American Chemical Society, Washington, DC, 2006, vol. 933, pp. 41–55.

33   L. A. Kaledin, A. L. Kaledin and M. C. Heaven, The electronic structure of the actinide oxides and their singly and doubly charged cations: A ligand field approach, *Int. J. Quantum Chem.*, , DOI:10.1002/qua.26588.

34   A. S. P. Gomes, F. Réal, B. Schimmelpfennig, U. Wahlgren and V. Vallet, in *Computational Methods in Lanthanide and Actinide Chemistry*, John Wiley & Sons Ltd, Chichester, UK, 2015, pp. 269–298.

35   J. Autschbach, N. Govind, R. Atta-Fynn, E. J. Bylaska, J. W. Weare and W. A. de Jong, in *Computational Methods in Lanthanide and Actinide Chemistry*, John Wiley & Sons Ltd, Chichester, UK, 2015, pp. 299–342.

36   V. Manchanda, P. Pathak and P. Mohapatra, in *Ion Exchange and Solvent Extraction A Series of Advances, Volume 19*, ed. B. A. Moyer, CRC Press, Philadelphia, 2009, pp. 65–118.

37   S. A. Ansari, P. Pathak, P. K. Mohapatra and V. K. Manchanda, Aqueous Partitioning of Minor Actinides by Different Processes, *Sep. Purif. Rev.*, 2011, **40**, 43–76.

38   J. D. Burns, M. Borkowski, A. Clearfield and D. T. Reed, Separation of oxidized americium from lanthanides by use of pillared metal(IV) phosphate-phosphonate hybrid materials, *Radiochim. Acta*, 2012, **100**, 901–906.

39   J. D. Burns, A. Clearfield, M. Borkowski and D. T. Reed, Pillared metal(IV) phosphate-phosphonate extraction of actinides, *Radiochim. Acta*, 2012, **100**, 381–387.

40   J. D. Burns, T. C. Shehee, A. Clearfield and D. T. Hobbs, Separation of Americium from Curium by Oxidation and Ion Exchange, *Anal. Chem.*, 2012, **84**, 6930–6932.

41   R. A. Wigeland, T. Taiwo and M. Todosow, in *Global 2015*, Paris, France, 2015, pp. 329–335.

42   M. Miguirditchian, L. Chareyre, X. Heres, C. Hill, P. Baron and M. Masson, in *GLOBAL 2007*, American Nuclear Society, La Grange Park, IL, 2007, pp. 550–552.

43   E. Aneheim, C. Ekberg, A. Fermvik, M. R. S. J. Foreman, T. Retegan and G. Skarnemark, A TBP/BTBP-based GANEX Separation Process. Part 1: Feasibility, *Solvent Extr. Ion Exch.*, 2010, **28**, 437–458.

44   B. J. Mincher, L. R. Martin and N. C. Schmitt, Tributylphosphate Extraction Behavior of Bismuthate-Oxidized Americium, *Inorg. Chem.*, 2008, **47**, 6984–6989.

45   C. J. Dares, A. M. Lapides, B. J. Mincher and T. J. Meyer, Electrochemical oxidation of 243Am(III) in nitric acid by a terpyridyl-derivatized electrode, *Science*, 2015, **350**, 652–655.

46   B. A. Moyer, G. J. Lumetta and B. J. Mincher, in *Reprocessing and Recycling of Spent Nuclear Fuel*, Elsevier, Cambridge, 2015, pp. 289–312.

47   K. McCann, D. M. Brigham, S. Morrison and J. C. Braley, Hexavalent Americium

Recovery Using Copper(III) Periodate, *Inorg. Chem.*, 2016, **55**, 11971–11978.

48   B. J. Mincher, R. D. Tillotson, T. Garn, V. Rutledge, J. Law and N. C. Schmitt, The solvent extraction of Am(VI) using centrifugal contactors, *J. Radioanal. Nucl. Chem.*, 2016, **307**, 1833–1836.

49   B. J. Mincher, N. C. Schmitt, B. K. Schuetz, T. C. Shehee and D. T. Hobbs, Recent advances in f-element separations based on a new method for the production of pentavalent americium in acidic solution, *RSC Adv.*, 2015, **5**, 27205–27210.

50   T. Shehee, L. R. Martin, P. R. Zalupski and K. L. Nash, Redox-Based Separation of Americium from Lanthanides in Sulfate Media, *Sep. Sci. Technol.*, 2010, **45**, 1743–1752.

51   J. D. Burns and B. A. Moyer, Group Hexavalent Actinide Separations: A New Approach to Used Nuclear Fuel Recycling, *Inorg. Chem.*, 2016, **55**, 8913–8919.

52   J. D. Burns and B. A. Moyer, Uranyl nitrate hexahydrate solubility in nitric acid and its crystallization selectivity in the presence of nitrate salts, *J. Clean. Prod.*, 2018, **172**, 867–871.

53   E. D. Kitcher and J. D. Burns, Criticality concerns of a group actinide co-crystallization separations approach to used nuclear fuel recycling, *Ann. Nucl. Energy*, 2018, **115**, 387–392.

54   W. H. Runde and B. J. Mincher, Higher Oxidation States of Americium: Preparation, Characterization and Use for Separations, *Chem. Rev.*, 2011, **111**, 5723–5741.

55   J. D. Einkauf and J. D. Burns, Solid state characterization of oxidized actinides co-crystallized with uranyl nitrate hexahydrate, *Dalt. Trans.*, 2020, **49**, 608–612.

56   J. D. Einkauf and J. D. Burns, Recovery of Oxidized Actinides, Np(VI), Pu(VI), and Am(VI), from Cocrystallized Uranyl Nitrate Hexahydrate: A Single Technology Approach to Used Nuclear Fuel Recycling, *Ind. Eng. Chem. Res.*, 2020, **59**, 4756–4761.

57   J. D. Einkauf and J. D. Burns, Interactions of the Bismuthate Anion with Alkali, Alkaline Earth, Lanthanide, and Actinide Metals in Nitric Acid Systems, *ACS Appl. Energy Mater.*, 2020, **3**, 1593–1601.

58   H. A. Friedman and L. M. Toth, Absorption spectra of Np(III), (IV), (V) and (VI) in nitric acid solution, *J. Inorg. Nucl. Chem.*, 1980, **42**, 1347–1349.

59   D. L. Clark, S. S. Hecker, G. D. Jarvinen and M. P. Neu, in *The Chemistry of the Actinide and Transactinide Elements*, Springer Netherlands, Dordrecht, 2010, pp. 813–1264.

60   E. Browne and R. B. Firestone, *Table of Radioactive Isotopes*, Wiley, New York, 1st edn., 1986.

61   M. Dolg, H. Stoll, H. Preuss and R. M. Pitzer, Relativistic and correlation effects for element 105 (hahnium, Ha): a comparative study of M and MO (M = Nb, Ta, Ha) using energy-adjusted ab initio pseudopotentials, *J. Phys. Chem.*, 1993, **97**, 5852–5859.

62   C. Lee, W. Yang and R. G. Parr, Development of the Colle-Salvetti correlation-energy formula into a functional of the electron density, *Phys. Rev. B*, 1988, **37**, 785–789.

63   A. D. Becke, Density-functional thermochemistry. III. The role of exact exchange, *J. Chem. Phys.*, 1993, **98**, 5648–5652.

64   E. J. Baerends, T. Ziegler, A. J. Atkins, J. Autschbach, O. Baseggio, D. Bashford, A. Bérces, F. M. Bickelhaupt, C. Bo, P. M. Boerrigter, L. Cavallo, C. Daul, D. P. Chong, D. V. Chulhai, L. Deng, R. M. Dickson, J. M. Dieterich, A. L. Ellis, D., M. v. Faassen, L. Fan, T. H. Fischer, C. F. Guerra, M. Franchini, A. Ghysels, A. Giammona, S. J. A. v. Gisbergen, A. Goez, A. W. Götz, J. A. Groeneveld, O. V. Gritsenko, M. Grüning, S. Gusarov, F. E. Harris, P. v. d. Hoek, Z. Hu, C. R. Jacob, H. Jacobsen, L. Jensen, L.

Joubert, J. W. Kaminski, G. v. Kessel, C. König, F. Kootstra, A. Kovalenko, M. V. Krykunov, E. v. Lenthe, D. A. McCormack, A. Michalak, M. Mitoraj, S. M. Morton, J. Neugebauer, V. P. Nicu, L. Noodleman, V. P. Osinga, S. Patchkovskii, M. Pavanello, C. A. Peeples, P. H. T. Philipsen, D. Post, C. C. Pye, H. Ramanantoanina, P. Ramos, W. Ravenek, J. I. Rodríguez, P. Ros, R. Rüger, P. R. T. Schipper, D. Schlüns, H. v. Schoot, G. Schreckenbach, J. S. Seldenthuis, M. Seth, J. G. Snijders, M. Solà, M. Stener, M. Swart, D. Swerhone, V. Tognetti, G. t. Velde, P. Vernooijs, L. Versluis, L. Visscher, O. Visser, F. Wang, T. A. Wesolowski, E. M. v. Wezenbeek, G. Wiesenekker, S. K. Wolff, T. K. Woo and A. L. Yakovlev, 2017.

65   R. L. Martin, Natural transition orbitals, *J. Chem. Phys.*, 2003, **118**, 4775–4777.

66   I. Fdez. Galván, M. Vacher, A. Alavi, C. Angeli, F. Aquilante, J. Autschbach, J. J. Bao, S. I. Bokarev, N. A. Bogdanov, R. K. Carlson, L. F. Chibotaru, J. Creutzberg, N. Dattani, M. G. Delcey, S. S. Dong, A. Dreuw, L. Freitag, L. M. Frutos, L. Gagliardi, F. Gendron, A. Giussani, L. González, G. Grell, M. Guo, C. E. Hoyer, M. Johansson, S. Keller, S. Knecht, G. Kovačević, E. Källman, G. Li Manni, M. Lundberg, Y. Ma, S. Mai, J. P. Malhado, P. Å. Malmqvist, P. Marquetand, S. A. Mewes, J. Norell, M. Olivucci, M. Oppel, Q. M. Phung, K. Pierloot, F. Plasser, M. Reiher, A. M. Sand, I. Schapiro, P. Sharma, C. J. Stein, L. K. Sørensen, D. G. Truhlar, M. Ugandi, L. Ungur, A. Valentini, S. Vancoillie, V. Veryazov, O. Weser, T. A. Wesołowski, P.-O. Widmark, S. Wouters, A. Zech, J. P. Zobel and R. Lindh, OpenMolcas: From Source Code to Insight, *J. Chem. Theory Comput.*, 2019, **15**, 5925–5964.

67   F. Aquilante, J. Autschbach, A. Baiardi, S. Battaglia, V. A. Borin, L. F. Chibotaru, I. Conti, L. De Vico, M. Delcey, I. Fdez. Galván, N. Ferré, L. Freitag, M. Garavelli, X. Gong, S. Knecht, E. D. Larsson, R. Lindh, M. Lundberg, P. Å. Malmqvist, A. Nenov, J. Norell, M. Odelius, M. Olivucci, T. B. Pedersen, L. Pedraza-González, Q. M. Phung, K. Pierloot, M. Reiher, I. Schapiro, J. Segarra-Martí, F. Segatta, L. Seijo, S. Sen, D.-C. Sergentu, C. J. Stein, L. Ungur, M. Vacher, A. Valentini and V. Veryazov, Modern quantum chemistry with [Open]Molcas, *J. Chem. Phys.*, 2020, **152**, 214117.

68   A. Wolf, M. Reiher and B. A. Hess, The generalized Douglas–Kroll transformation, *J. Chem. Phys.*, 2002, **117**, 9215–9226.

69   B. O. Roos, P. R. Taylor and P. E. M. Sigbahn, A complete active space SCF method (CASSCF) using a density matrix formulated super-CI approach, *Chem. Phys.*, 1980, **48**, 157–173.

70   J. Finley, P.-Å. Malmqvist, B. O. Roos and L. Serrano-Andrés, The multi-state CASPT2 method, *Chem. Phys. Lett.*, 1998, **288**, 299–306.

71   F. Gendron, D. Páez-Hernández, F.-P. Notter, B. Pritchard, H. Bolvin and J. Autschbach, Magnetic Properties and Electronic Structure of Neptunyl(VI) Complexes: Wavefunctions, Orbitals, and Crystal-Field Models, *Chem. - A Eur. J.*, 2014, **20**, 7994–8011.

72   T. J. Duignan and A. Marchenko, .

73   B. Ravel and M. Newville, ATHENA , ARTEMIS , HEPHAESTUS : data analysis for X-ray absorption spectroscopy using IFEFFIT, *J. Synchrotron Radiat.*, 2005, **12**, 537–541.

74   J. C. Taylor and M. H. Mueller, A neutron diffraction study of uranyl nitrate hexahydrate, *Acta Crystallogr.*, 1965, **19**, 536–543.

75   R. Kawashima, M. Sasaki, S. Satoh, H. Isoda, Y. Kino and Y. Shiozaki, Report on Temperature Dependence of Crystal Structure for Samarium Nitrate Having Metastable

Phenomena, *J. Phys. Soc. Japan*, 2000, **69**, 3297–3303.

76   C. Riddle, K. Czerwinski, E. Kim, P. Paviet, P. Weck, F. Poineau and S. Conradson, Characterization of pentavalent and hexavalent americium complexes in nitric acid using X-ray absorption fine structure spectroscopy and first-principles modeling, *J. Radioanal. Nucl. Chem.*, 2016, **309**, 1087–1095.

77   C. Riddle and L. R. Martin, in *U.S. Department of Energy Material Recovery and Waste Form Development*, Idaho National Laboratory, 2014.

78   H. A. Thompson, G. E. Brown and G. A. Parks, XAFS spectroscopic study of uranyl coordination in solids and aqueous solution, *Am. Mineral.*, 1997, **82**, 483–496.

79   A. Ikeda, C. Hennig, A. Rossberg, S. Tsushima, A. C. Scheinost and G. Bernhard, Structural Determination of Individual Chemical Species in a Mixed System by Iterative Transformation Factor Analysis-Based X-ray Absorption Spectroscopy Combined with UV−Visible Absorption and Quantum Chemical Calculation, *Anal. Chem.*, 2008, **80**, 1102–1110.

80   P. Lindqvist-Reis, C. Apostolidis, O. Walter, R. Marsac, N. L. Banik, M. Y. Skripkin, J. Rothe and A. Morgenstern, Structure and spectroscopy of hydrated neptunyl(vi) nitrate complexes, *Dalt. Trans.*, 2013, **42**, 15275.

81   A. J. Gaunt, I. May, M. P. Neu, S. D. Reilly and B. L. Scott, Structural and Spectroscopic Characterization of Plutonyl(VI) Nitrate under Acidic Conditions, *Inorg. Chem.*, 2011, **50**, 4244–4246.

82   K.-A. Hughes and P. C. Burns, Uranyl dinitrate trihydrate, UO 2 (NO 3) 2 (H 2 O) 3, *Acta Crystallogr. Sect. C Cryst. Struct. Commun.*, 2003, **59**, i7–i8.

83   P. Lindqvist-Reis, C. Apostolidis, J. Rebizant, A. Morgenstern, R. Klenze, O. Walter, T. Fanghänel and R. G. Haire, The Structures and Optical Spectra of Hydrated Transplutonium Ions in the Solid State and in Solution, *Angew. Chemie Int. Ed.*, 2007, **46**, 919–922.

84   L. Soderholm, C. Williams, S. Skanthakumar, M. R. Antonio and S. Conradson, The synthesis and characterization of the superconductor-related compound Pb2Sr2AmCu3O8, *Zeitschrift für Phys. B Condens. Matter*, 1996, **101**, 539–545.

85   J. A. Bearden and A. F. Burr, Reevaluation of X-Ray Atomic Energy Levels, *Rev. Mod. Phys.*, 1967, **39**, 125–142.

86   D.-C. Sergentu, T. J. Duignan and J. Autschbach, Ab Initio Study of Covalency in the Ground versus Core-Excited States and X-ray Absorption Spectra of Actinide Complexes, *J. Phys. Chem. Lett.*, 2018, **9**, 5583–5591.

87   N. A. Meredith, M. J. Polinski, J. N. Cross, E. M. Villa, A. Simonetti and T. E. Albrecht-Schmitt, Synthetic Influences on Neptunium Incorporation in Naturally Occurring Copper Uranyl Phosphates, *Cryst. Growth Des.*, 2013, **13**, 386–392.

88   Y. N. Heit, F. Gendron and J. Autschbach, Calculation of Dipole-Forbidden 5f Absorption Spectra of Uranium(V) Hexa-Halide Complexes, *J. Phys. Chem. Lett.*, 2018, **9**, 887–894.

89   G. Ganguly, H. D. Ludowieg and J. Autschbach, Ab Initio Study of Vibronic and Magnetic 5f-to-5f and Dipole-Allowed 5f-to-6d and Charge-Transfer Transitions in [UX 6] n − (X = Cl, Br; n = 1, 2), *J. Chem. Theory Comput.*, 2020, **16**, 5189–5202.

90   G. Ganguly, D. Sergentu and J. Autschbach, Ab Initio Analysis of Metal–Ligand Bonding in An(COT) 2 with An=Th, U in Their Ground- and Core-Excited States, *Chem. – A Eur. J.*, 2020, **26**, 1776–1788.

Table of Contents Graphic and Text
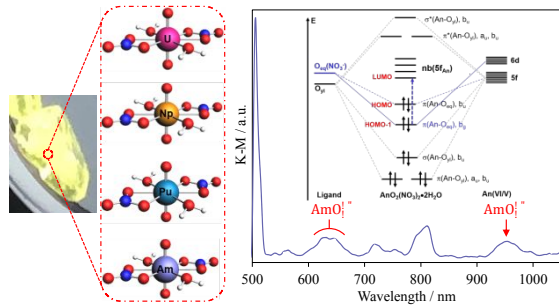
The solid-state electronic structure of oxidized actinides was probed by co-crystallization Np(VI), Pu(VI), Am(VI), as well as Np(V), with $UO_2(NO_3)_2 \cdot 6H_2O$. Comprehensive analysis of the solid-state diffuse reflectance UV-Vis-NIR absorption spectra were carried out and coupled with theoretical calculations. Additional characterization of the products was performed via SEM-EDS and EXAFS measurements.